Taylor & Francis
Taylor & Francis Group

Science and Technology of Advanced Materials: Methods

ISSN: 2766-0400 (Online) Journal homepage: www.tandfonline.com/journals/tstm20

A design methodology of crystal growth furnace and process aided by two-step optimization using machine learning models and genetic algorithm

Hiroyuki Tanaka, Kentaro Kutsukake, Kota Asakura, Takuto Kojima, Xin Liu & Noritaka Usami

To cite this article: Hiroyuki Tanaka, Kentaro Kutsukake, Kota Asakura, Takuto Kojima, Xin Liu & Noritaka Usami (28 Oct 2025): A design methodology of crystal growth furnace and process aided by two-step optimization using machine learning models and genetic algorithm, Science and Technology of Advanced Materials: Methods, DOI: 10.1080/27660400.2025.2581358

To link to this article: https://doi.org/10.1080/27660400.2025.2581358

Publisher: Taylor & Francis & The Author(s). Published by National Institute for Materials Science in partnership with Taylor & Francis Group
Journal: *Science and Technology of Advanced Materials: Methods*
DOI: 10.1080/27660400.2025.2581358

A design methodology of crystal growth furnace and process aided by two-step optimization using machine learning models and genetic algorithm

Hiroyuki Tanaka[a], Kentaro Kutsukake[a,b,c], Kota Asakura[a], Takuto Kojima[d], Xin Liu[b], and Noritaka Usami[a,b,e*]

[a]*Graduate School of Engineering, Nagoya University, Furo-cho, Chikusa-ku, Nagoya 464-8603, Japan*

[b]*Institute of Materials and Systems for Sustainability, Nagoya University, Furo-cho, Chikusa-ku, Nagoya 464-8601, Japan*

[c] *Center of Advanced Intelligence Project, RIKEN, Tokyo 103-0027, Japan*

[d] *National Institute of Advanced Industrial Science and Technology, Tsukuba 305-8561, Japan*

[e] *Institutes of Innovation for Future Society, Nagoya University, Furo-cho, Chikusa-ku, Nagoya 464-8601, Japan*

[*]E-mail: usa@material.nagoya-u.ac.jp

A design methodology of crystal growth furnace and process aided by two-step optimization using machine learning models and genetic algorithm

We have developed an innovative design method for crystal growth furnaces and processes involving two-step optimization. The first step focuses on finding the ideal temperature transition around the crucible without assuming a specific crystal growth furnace. The design of the crystal growth furnace and process is then optimized to replicate the ideal temperature transition. We utilized a deep neural network model in each optimization step to substitute crystal growth simulation and genetic algorithm. A proof-of-concept optimization is performed for the directional solidification of a crystalline silicon ingot in a crucible. Since our method does not rely on a predetermined furnace, we can achieve more flexible temperature distribution transitions than conventional approaches by implementing adaptable temperature boundary conditions. This allows us to refine the design of the crystal growth furnace and process, which has significant potential to advance the production of a wide range of materials and improve materials production environments and equipment design.

Keywords: optimization, machine learning, genetic algorithm, crystal growth, process informatics

1. Introduction

The optimization of manufacturing processes for materials can be quite challenging due to the vast and complex parameter space involved [1–4]. Even seemingly simple processes, such as growing bulk crystals from a melt, can have numerous variations of process parameters to result in various crystal qualities [5–9]. These variations in process parameters include temperature distribution and its changes over time, component materials and their geometry, and the pre-treatment of raw materials. Moreover, the interaction between these parameters makes the relationship between process parameters and crystal quality extremely complex, making optimization difficult. To address these issues, optimization has conventionally been performed by repeating the cycle of crystal growth, crystal evaluation, and verification of growth

conditions based on the evaluation results. This process relies on the fundamental knowledge, empirical rules, and know-how of experts. However, this cycle requires even skilled experts to conduct a certain number of experiments due to the vast and complex parameter space, making the trial-and-error process costly in terms of time and money. Therefore, innovative efforts to decrease the time and cost of optimization through data-driven experiments, exemplified by Bayesian optimization, are advancing in various fields [10–16].

On the other hand, multi-physics simulation, which considers multiple physical phenomena, has become a common approach for designing crystal growth conditions [17–23]. Simulation helps narrow down the growth conditions to some extent, and optimal conditions can often be found with fewer experiments than before. Additionally, informatics applications are thriving, and advancements in process informatics are transforming optimization methods. It has been reported that many process parameters can be optimized quickly by creating machine learning models that can predict simulation results instantly and then applying mathematical optimization algorithms [24–28]. It should be remarked that most of these efforts have focused on assuming a specific crystal growth furnace and optimizing numerically adjustable parameters within the constraints of that furnace. Since attempts to apply machine learning to the design of a furnace have been very limited [29,30], the optimal conditions obtained may be locally optimal solutions based on the assumed constraints. By removing the constraint of using a specific crystal growth furnace, it may be possible to find conditions (such as the varying temperature distribution over time) that could lead to better crystals. In other words, we must simultaneously conduct furnace design and process optimization to realize ideal quality crystals.

In this research, we propose a two-step optimization method, as illustrated in Fig. 1. First, we will search for ideal growth conditions without being limited by the specific furnace constraints. Then, we will design a furnace to achieve these growth conditions. To demonstrate the usefulness of this method, we will use the directional growth of silicon ingots in a crucible as a model system. In the first stage, we will create a machine learning model to predict crystal quality based on the time variation of the temperature distribution around the crucible periphery during the crystal growth process. Using mathematical optimization algorithms, we will then determine the ideal time

variation of the temperature distribution to achieve high-quality crystals. In the second step, we will parameterize the internal structure of the crystal growth furnace and create a machine learning model to predict the time variation of temperature based on the structural parameters and the crucible position. This model will provide the appropriate time variation of the crucible position in order to minimize the deviation from the ideal temperature distribution. [Figure 1. near here]

2. Optimization of the crystal growth process

2.1: Computational model for material surroundings

To achieve the optimal temperature distribution around the crystal without constraints from the growth furnace structure, a calculation model focused on the material surroundings was developed. We created a calculation model specifically focusing on the environment around the crystalline silicon as shown in Fig. 2. This "crucible model" was utilized to conduct non-stationary calculations by providing a time series of temperature boundary conditions on all four sides. For the simulations, a commercial crystal growth simulator CGSim, provided by STR Japan K.K., was employed. This software package enables the calculation of the entire thermal process, from melting to cooling. Heat transfer among the components of the furnace, through heat conduction, thermal radiation, and melt convection, significantly affects the heat transport. Consequently, an axisymmetric two-dimensional cylindrical and unsteady comprehensive heat transfer analysis was conducted to consider these factors in all components of the crucible model. Moreover, unsteady calculations were performed for the entire solidification and cooling processes to predict changes in dislocation density and residual stress within the crystal [31,32]. The physical properties of silicon used for the simulation are summarized in Table I. [Figure 2. near here] [Table I. near here]

2.2: Generation of temperature boundary conditions

Using the crucible model, we statistically investigated the relationship between the solid-liquid interface shape, growth rate, and dislocation density by applying various time-series temperature boundary conditions around the crucible, assuming the crystal growth and cooling processes, and performing unsteady calculations. First, the melting

process (0-7 hours) was analyzed unsteadily using the crucible model, and the results at 7 hours were used as the initial conditions. For the crystal growth and cooling processes, the temperature boundary conditions were randomly given around the crucible within realistic constraints to generate the training data for machine learning. The method of generating the realistic temperature boundary conditions is as follows. First, 13 nodes were selected from the 174 nodes around the crucible, and the temperatures were randomly generated with a constrained quartic function in temporal transition as expressed by equation (1). Boucetta *et al.* used artificial neural networks to perform optimization of the temperature sensor locations to predict the temperature distribution in the furnace accurately and found that attention should be paid to the vicinity of material boundaries[33]. Considering their significant impact, we selected the nodes at the locations shown in Fig.3(a). This includes monitoring the temperatures near the bottom of the crucible and the top of the ingot. [Figure 3. near here]

The constraints of the quartic function are expressed as the following equations (2)-(6).

$$f(t) = \sum_{n=0}^{4} a_n t^n \#(1)$$

$$f(t_0) = T_0 \#(2)$$

$$f(t_{end}) = T_{end} \#(3)$$

$$\left.\frac{df}{dt}\right|_{t=0} = \Delta T_0 \#(4)$$

$$f(t_{end}) \le f(t) \le f(t_0) \#(5)$$

$$f(t_{solid}) \ge T_i \#(6)$$

$f(t)$ represents the temperature time series data generated by the quartic function. t_0 represents the start time of the crystal growth process, t_{end} represents the end time of the cooling process, T_0 and T_{end} represent the initial and final temperature of the crystal growth process, and T_i represents the lower temperature limit of each node i at t_{solid}. ΔT_0 is temperature transition speed at the end of the melting process.

The main constraints include fixed initial and final temperatures, continuity during the melting process, and a defined temperature range, as expressed in Eqs. (2) to (5). These constraints are essential for controlling the temperature gradient in the growth direction, preventing remelting, which is characteristic of the directional solidification process,

and ensuring experimental reproducibility. For the temperature range, upper and lower limits are established along with a specific lower temperature threshold for each node at a given time, t_{solid}, as expressed in Eq. (6). This constraint is crucial for preventing rapid crystallizations. In this study, t_{solid} and T_i were set to ensure a crystallization rate of no more than 0.35 mm/min. Without this limitation, the crucible would cool too quickly, resulting in crystallization from the upper section and uncontrolled dislocation propagation. Consequently, simulations often fail to converge. While this constraint reflects a realistic condition, it is also vital for efficient data generation. However, if the constraints are too strict, they may reduce the search space and lead to the overlooking of optimal solutions. Therefore, it is important to balance realistic constraints with a broad exploration of conditions.

Figure 3(b) shows an example of the generation of temperature boundary conditions. The temperature boundary conditions for the remaining 161 nodes were then obtained by cubic spline interpolation. Using the temperature boundary conditions generated by the above procedure, an axisymmetric two-dimensional transient simulation was performed assuming various temperature distribution transitions independent of the growth furnace geometry.

2.3: Construction of DNN model

A deep neural network (DNN) model was constructed to explore the correspondence between crucible wall temperature and ingot quality characteristics. Figure 4 shows the structure of the DNN model constructed (hereinafter referred to as Model A). Temporal temperature profiles and mesh coordinates (r, z) of the ingot region (62 × 108 points) at 13 locations on the crucible wall were selected as inputs for Model A. The temporal temperature profiles were selected every 20 minutes for 600 minutes from the start of crystal growth. Thus, a total of 390 temperature values (30 time steps × 13 positions) were input to the DNN. The temperature profiles were entered after normalization using the upper and lower temperature limits set during the generation of the temperature profiles at each location. The hidden layer consisted of 150 nodes × 5 layers. The output was the dislocation density and solidification time for each grid (r, z) of the silicon ingot at the end of crystal growth. The dislocation density was designed to be output in normal logarithm. The Adaptive Moment Estimation (Adam) method

included in TensorFlow was used as the optimization algorithm. ReLU was used as the activation function, which is a nonlinear function that outputs the input as it is if the input is above 0 and outputs 0 if the input is below 0. [Figure 4. near here]

Using the crucible model, we conducted 211 sets of simulations with 390 different combinations of temperature variations to generate the training data for Model A. The output data included 211 sets of dislocation density and crystallization time, with a total of (62 × 108) data points. We performed five-fold cross-validation to train and evaluate the neural network for Model A.

Figure 5 compares the simulation results with the predictions of Model A. Model A was well-trained and could instantly predict the crystallization time required for silicon ingot growth, as well as the interface geometry during crystal growth, and the dislocation density. Figure 6 shows parity plots to evaluate the prediction accuracy of Model A for all test data. It is evident that both (a) the crystallization time and (b) the distribution of dislocation density were predicted with high accuracy. The average R2 scores from five-fold cross-validation for the crystallization time and the logarithm of dislocation density were 0.997 and 0.881, respectively. A summary of each R2 score, mean absolute error (MAE), and mean squared error (MSE) for the five-fold cross-validation models is presented in Table S1 in the Supplemental. The lower prediction accuracy for dislocation density compared to crystallization time can be attributed to the lack of high dislocation density data. Under certain temperature boundary conditions, regions with extremely high dislocation densities, exceeding 10^{10} cm^{-2}, can develop locally. However, since these regions rarely occur under the conditions used to generate the training data for this study, there is limited data on such high dislocation densities, resulting in decreased average prediction accuracy. Nonetheless, the focus of this study is to identify conditions that lead to low dislocation density, making the lack of high dislocation density data less critical for our objectives.

It should be remarked that the simulation of a 10-hour process in CGSim takes about 7 hours (25200 seconds). On the other hand, the constructed Model A outputs the same result in about 800 microseconds. This means that the constructed machine learning model is able to obtain the same results as the simulation 31.5 million times faster. [Figure 5. near here][Figure 6. near here]

2.4: Optimization of temperature distribution transition by genetic algorithm

The genetic algorithm (GA) was applied to obtain the optimal crucible wall temperature distribution transition: NSGA-II[34], an algorithm developed by Debet *et al.* and capable of multi-objective optimization, was employed in this study [34]. GA inherently requires a large number of evaluations, making it less efficient compared to methods like Bayesian optimization. However, GA is less likely to get stuck in local optima, making it effective for finding global solutions. This advantage is particularly noteworthy in scenarios where a machine learning model supports rapid, large-scale evaluations, as shown in previous studies [25-27, 30].

Since 390 temperatures (30 time steps at 13 locations) were considered too time-costly to optimize, we focused on the temperature coefficients of the constrained quartic function used in the data generation. In the constrained quartic function, two coefficients can describe the temperature transition at each location because of the three strong constraints Eqs. (2)-(4) for five variables. Therefore, there are 26 parameters to be optimized, representing temperature transitions at 13 locations. Before proceeding with the optimization, it is beneficial to examine the correlation of the regression coefficients for possible further dimensionality reduction and interpretation of the optimization results. Figure 7 shows a scatter plot of the two coefficients at 13 locations for the temperature transient used in the training data generation. The red line in the figure is the linear regression result, and each graph shows the R2 score of the linear regression. It is obvious that there is strong linearity for the pairs of polynomial coefficients at all 13 locations. This may be due to the limit constraints of Eqs. (5) and (6) imposed on the temperature data generation. Therefore, we worked on optimizing 13 polynomial coefficients, one for each position, for a total of 13. [Figure 7. near here]

Figure 8 shows the workflow of the GA in conjunction with Model A. NSGA-II solved the minimization problem with three objective functions: the mean value of dislocation density, the maximum value of dislocation density, and the crystallization time. Specifically, 1000 random individuals were generated within the range of parameters used in the training data of Model A. After 200 generations of changes, the optimal combinations of parameters were proposed. In each optimization loop, 13 polynomial coefficients suggested by NSGA- II were substituted into the constrained quartic function to obtain time series temperature data at the 13 selected locations. Then,

the objective functions were calculated through Model A using the time series temperature. The entire optimization process was completed in less than six hours thanks to fast prediction by machine learning models, and the obtained solution was well converged, as shown in Fig. S1 in the Supplemental. [Figure 8. near here]

Figure 9 shows the Pareto surfaces for crystallization time, average dislocation density, and maximum dislocation density obtained through the NSGA-II. After 200 generations, the Pareto front shifted to the lower left compared to the initial cluster. This supports the effectiveness of optimization through GA. For furnace optimization, we should select a target solution from model B, which is represented in the Pareto front consisting of 1000 individuals. When choosing this solution, it is crucial to consider the implications of extrapolation. Solutions with shorter solidification times fall outside the range of the training data, leading to frequent computational infeasibility in simulations. Therefore, we avoided solutions located in the extrapolation range and instead opted for the solution anticipated to yield the minimum maximum dislocation density. This solution is indicated by stars in Figure 9.

[Figure 9. near here]

We conducted simulations using the optimal temperature distribution transition derived from a set of optimal parameters, focusing on the crucible wall temperature. Figure 10 displays the ideal temperature distribution on the side wall of the crucible. While the overall temperature is lowered with time to promote crystallization, the temperatures at the 0 mm and 10 mm positions behave quite differently. The temperature at the 0 mm position increases during the post-growth stage. This increase is intended to reduce the post-solidification temperature difference between the top and bottom of the crystal ingot, thereby mitigating thermal stress. In contrast, the temperature at the 10 mm position rises during the middle to late stages of the growth. By elevating the temperature of the lower crucible side region, heat removal from the bottom-side surfaces is suppressed, making heat flux through the bottom surface predominant. Both temperature transients help to suppress the multiplication of dislocations. In Fig. 11, we compare the average growth rate and dislocation density at the center of the ingot using the original recipe and post-optimization results. It is noted

that the “original recipe” refers to the parameter set usually used in the authors' group, which has been optimized through actual experimental trials and errors. Thus, the simulation result of the original recipe is much better than that of the randomly generated training data. The optimized temperature distribution transition exhibits a rapid growth rate in the early stage. Additionally, the original recipe shows an increase in dislocation density towards the top of the ingot, while this increase is mitigated in the optimized transition. As mentioned above, in crystal growth with the optimal temperature distribution, we observed heating of the bottom-side wall of the crucible during the middle to late stages of the growth. This heating appears to have limited heat dissipation from the side wall, consequently reducing the crystal growth rate near the side wall. This suppression of heat removal led to a decrease in the generation of dislocations, as well as a reduction in the temperature difference in the radial direction of the ingot. Notably, the temperature difference at the top of the ingot in the final stage of crystal growth was 24 K in the original recipe and reduced to 8 K in the optimal temperature distribution transition. These findings indicate that the optimal temperature distribution effectively reduced the temperature gradient in the radial direction during the late growth stage, resulting in a lower dislocation density. [Figure 10. near here] [Figure 11. near here]

Furthermore, a correlation analysis was performed not only on the optimal solution but also on the entire training data generated in this study to investigate the influence of temperature at each position around the crucible. Figure 12 shows the correlation coefficient matrix between the polynomial coefficients and the objective functions, i.e., crystallization time, the maximum dislocation density, and the average dislocation density. The subscripts correspond to the position shown in Fig.2 :1-3 in the polynomial coefficients refer to the three nodes in the upper part of the model, starting from the center; 4-10 refer to the seven nodes in the side part of the model, starting from the bottom; 11-13 correspond to the three nodes in the lower part of the model. The crystallization time is correlated with the polynomial coefficients at nodes a1-a3 and a9-a10, which corresponds to the upper part of the computational model. The average and maximum dislocation densities are strongly correlated with the polynomial coefficients at nodes a4-a7 in the lower part of the side of the calculation model. This may indicate that the radial temperature gradient from the beginning to the middle of crystal growth

has a strong influence on the size of the average dislocation density. In addition, the correlation coefficient between crystallization time and dislocation density has an opposite sign, suggesting a trade-off relationship between fast growth and low dislocation density. As demonstrated in these analyses, systematic data generation for temperature distribution transient using quartic function and constraints is useful for capturing the tendency of the parameter influence. [Figure 12. near here]

3. Optimization of the growth furnace design

3.1: Screening of crystal growth furnace geometry parameters

We are in the process of designing a crystal growth furnace to achieve optimized temperature distribution obtained in Chapter 2. First, we conducted a thorough screening of various parameters related to the furnace to understand how the furnace design affects the temperature around the crucible and to reduce the optimization parameters. More simulations are needed to create machine learning models to optimize more parameters. Thus, we focused on the most influential parameters to streamline the optimization process. We selected seven structural parameters inside the crystal growth furnace that had been expected to impact the temperature distribution around the crystal and used an L18 orthogonal table for efficient screening.

Figure 13(a) illustrates the geometry inside the crystal growth furnace. By performing transient simulations with different parameter values in L18 orthogonal table f, we obtained the temperature distribution around the crucible. We used the simulation results to construct a multiple regression model and then calculated the root mean square errors (RMSE) for 13 temperature transient at different points around the crucible. This allowed us to analyze the impact of each parameter on the temperature distribution around the crystal. The regression coefficients in the multiple regression model show how the independent variables are related to the dependent variable. In our results, we found that the crucible table radius (r_c) and graphite table (t_g) had smaller effects compared to the other variables as shown in Fig.13(b). As a result, we focused on optimizing the model using the remaining five variables and constructing a nonlinear DNN model to use in the optimization process. [Figure 13. near here]

3.2: Construction of DNN model with input of selected parameters

In order to explore the relationship between the parameters related to the apparatus structure, crucible movement speed, and the temperature distribution around the crucible during crystal growth, we worked on the construction of a DNN model. For the parameters related to the apparatus structure, five parameters were selected for optimization based on the screening results: core tube width d_t, crucible base thickness t_c, insulation material diameter di, insulation material thickness t_i, and susceptor diameter r_s. The temperature of the heaters outside the core tube were fixed focusing on the furnace design. For the crucible movement speed, time series data of crucible position were used as the optimization target. Specifically, the crucible position was expressed as a constrained quartic function of time t, and its coefficients were used for optimization. The equation satisfied by the constrained quartic function is shown below.

$$f(t) = \sum_{n=0}^{4} a_n t^n \#(7)$$
$$f(t_0) = P_0 \#(8)$$
$$f(t_{\text{end}}) = P_{\text{end}} \#(9)$$
$$v_{\text{min}} \leq \frac{df}{dt} \leq v_{\text{max}} \#(10)$$
$$f(t_{\text{end}}) \leq f(t) \leq f(t_0) \#(11)$$

The function $f(t)$ represents the time series of the vertical position of the crucible generated by a quartic function. The initial time of the crystal growth is denoted as t_0, and the end time of crystal growth by the optimal temperature distribution transition is denoted as t_{end}. The crucible movement speed, represented by $\frac{df}{dt}$, was set within a range with the lower limit v_{min} = -10 mm/min and the upper limit v_{max} = 1 mm/min, which is the empirically determined range where we can grow crystals without cracking. The degree of freedom of the quartic function is 5, but by imposing the above constraint, the degree of freedom becomes 3. In other words, the crucible movement speed can be expressed by three variables.

In order to build the DNN of model B, we conducted 238 simulations with varying furnace designs and crucible movement speeds using CGSim software with an axisymmetric two-dimensional cylindrical model. Since our objective function to be optimized is the temperature distribution around the crucible, we performed only unsteady thermo-fluid calculations without coupling with time-consuming stress

analysis and dislocation propagation calculations. On the other hand, the simulations should start from room temperature because the melting process depends on the furnace design, while the crucible model can start with the same initial state just after the melting. Table II displays the parameter ranges and the number of partitions utilized to create the training data. Additionally, Figure 14 illustrates some of the time trends of the crucible positions used in the training data. The high degree of freedom allows for not only monotonically movements but also complex movements that combine descents and ascents. [Table II. near here] [Figure 14. near here]

The structure of a DNN model, referred to as Model B, is shown in Fig. 15. Model B takes the input parameters related to the five furnace designs, the vertical coordinates of the crucible, and the experimental time, all of which have been normalized. The hidden layer of Model B consists of 100 nodes across 5 layers. The outputs are the temperatures at 13 selected locations, which are the inputs of Model A. By including the experimental time as one of the input layers, this model can provide the temperatures at 13 locations at any given time. We used the Adam optimization algorithm in TensorFlow and employed the ReLU activation function. [Figure 15. near here]

The average R2 score for the five-fold cross-validation models of Model B was 0.808. Each R2 score, MAE, and MSE for the five-fold cross-validation models are summarized in Table S2 in the Supplemental. In Fig. 16, the simulation results, which are testing data not used for the DNN training, are compared with the predictions from Model B. It is evident that Model B is well-trained and can rapidly predict the optimal temperature distribution around the crucible. It is worth noting that the simulation by CGSim takes about 6 hours for a time-transient calculation. In contrast, Model B produces the same results in about 800 microseconds, which means it is possible to obtain almost the same results as the simulation 27 million times faster. This allows for the exploration of a huge number of parameter combinations in the following optimization. [Figure 16. near here]

3.3 Optimization of the geometry of the crystal growth furnace by genetic algorithm

Figure 17 shows the workflow of the GA in conjunction with Model B. NSGA-II aimed to minimize the difference from the temperature distribution transition around the

crucible optimized in Capter 2. NSGA-II generated 1000 random individuals as initial values within the range of parameters used in the training data for Model B, and 200 generations of changes, and proposed optimal parameter combinations to minimize the objective functions. The obtained solution was well converged, as shown in Fig. S2 in the Supplemental. 5 parameters related to the furnace design and 3 polynomial coefficients for the crucible movement were obtained. By substituting the obtained polynomial coefficients into the constrained quartic function shown in Equation (7), the time series of the vertical coordinates of the crucible was obtained. By inputting parameters related to the furnace design, vertical coordinates, and time into Model B, temperature transitions at 13 locations around the crucible were predicted, and each objective function was calculated from the prediction results. The vertical coordinate transition of the crucible was designed to satisfy following constraints: the upper and lower bounds of the vertical coordinate and the upper and lower bounds of the crucible movement speed. [Figure 17. near here]

Table III displays the parameters of the furnace design for the solution selected from the Pareto front, considering the importance of crucible wall temperature. Additionally, Figure 18 illustrates the time evolution of the vertical coordinates of the crucible. A noteworthy finding regarding the movement of the crucible indicates that it should be rapidly lowered in the early stage and raised in the late stage of the growth phase. These finding aligns with the results of the temperature transition optimization conducted in Chapter 2, which did not assume a specific furnace structure and demonstrated an increase in temperature during the late growth phase. [Table III. near here] [Figure 18. near here]

To evaluate the performance of the finally optimized furnace design and process conditions obtained by the proposed optimization sequence, we performed high-fidelity simulations with stress analysis and dislocation calculations, which are not incorporated in the simulations to generate training data for Model B. The results are shown in Figure 19. The dislocation density obtained with optimal furnace design and process conditions is lower than the original one, supporting the effectiveness of our optimization sequence. It is important to note that the differences in results between Model B and Model A stem from the variations in their simulation setups. The crucible model for Model A starts with the same initial conditions just after the melting process. Even though the

continuous constraint on the temperature tangent shown in Equation (4) was adopted, the rapid temperature change at the initial stage of the growth phase leads to the generation of dislocations. On the other hand, the simulation for Model B starts from the room temperature and continues to the growth phase, which results in a lower dislocation density.

In this way, it was demonstrated that process development, including equipment design, is possible by optimizing the temperature distribution transition without assuming a specific equipment structure as the first step and the furnace structure and crucible movement as the second step.

In the final section of this paper, we discuss the advantages, challenges and applicability associated with the proposed two-step optimization approach. One significant advantage of this method is the potential for model reuse. In this study, Model B was employed to model and optimize the effects of changes in the geometry inside the crystal growth furnace, such as the diameter of the crucible susceptor and the bottom thermal insulators, as well as the temporal variation in the crucible position. It should be noted that these were optimized under limited constraints and several assumptions, and they may not represent the global optimum considering all degrees of design freedom. In other words, several parameters remain to be optimized. Equipment design includes additional structural elements, such as the shape of the thermal insulators outside the core tube, and process parameter optimization involves temporal transitions in heater powers. Thus, future optimization efforts must address these parameters as well. Crucially, Model A retains its universal applicability. The only requirement is to develop a new Model B that considers the new parameters, enabling optimization to achieve the ideal conditions identified by Model A. The two-step optimization approach proposed in this study provides a versatile framework capable of accommodating various optimization scenarios.

On the other hand, a significant challenge in the two-step optimization approach lies in designing meaningful and feasible constraints for the boundary conditions of Model A while maintaining flexibility. In this study, the boundary conditions for Model A involved the temporal variation of the crucible's peripheral temperatures. To ensure unidirectional solidification from the bottom, constraints as expressed by equations (2) to (6) were applied while maintaining flexibility. If the constraints are too stringent, the

potential to identify optimal conditions is restricted; conversely, overly lenient constraints may yield unrealistic conditions. Thus, achieving an optimal balance is essential. Currently, designing these constraints requires specialized knowledge of the equipment, which poses a challenge. In the future, developing a framework for constraint design based on more diverse data is anticipated.

The two-step optimization proposed in this study can be applied not only to unidirectional solidification of multicrystalline silicon but also to a wide range of crystal growth processes. For example, in the Czochralski method for bulk crystal growth, we can optimize the internal structure of the furnace to achieve an ideal solid–liquid interface shape. This can be done by setting the crucible exterior and crystal surroundings as intermediate boundary conditions, performing inner-model optimization, and then designing the furnace structure accordingly. Similarly, in vapor-phase growth aimed at achieving uniform film thickness and composition, we could position a boundary closer to the substrate than the gas inlet. The gas flux across this boundary would be optimized first, and then the gas flow channels would be designed to realize the optimized flux profile.

By using carefully selected boundary conditions, high-degree-of-freedom optimizations, as demonstrated here, can become feasible. However, as mentioned earlier, this approach requires advanced expertise to define the appropriate boundaries and constraints. Therefore, the future development of support tools for designing boundary conditions is highly desirable.

4. Conclusion

We have developed a method for designing growth equipment and the growth process to produce high-quality crystals using simulation and machine learning. This allows for the exploration of optimal crystal growth conditions without being tied to specific growth equipment. We combined computational, machine learning, and mathematical optimization models to optimize the temperature distribution around the crucible and the growth furnace design. As a result, we discovered effective recipes for increasing the temperature and adjusting the crucible position during the late growth stage. The design method for manufacturing equipment introduced in this study can be applied not only to the growth of crystalline silicon, but also to various manufacturing methods and

equipment for other materials. This enables the development of processes, including equipment design, which has been challenging with traditional methods. We believe that our research will contribute to the advancement of process informatics.

Acknowledgement

This work was partly supported by JST CREST (JPMJCR17J1).

Data availability

The data that support the findings of this study are available upon reasonable request.

References

[1] Gao W, Zhang Y, Ramanujan D, et al. The status, challenges, and future of additive manufacturing in engineering. Computer-Aided Design. 2015;69:65–89.
[2] Herzog D, Seyda V, Wycisk E, et al. Additive manufacturing of metals. Acta Mater. 2016;117:371–392.
[3] Ngo TD, Kashani A, Imbalzano G, et al. Additive manufacturing (3D printing): A review of materials, methods, applications and challenges. Compos B Eng [Internet]. 2018;143(February):172–196.
[4] Kutsukake K, Nagai Y, Horikawa T, et al. Real-time prediction of interstitial oxygen concentration in Czochralski silicon using machine learning. Applied Physics Express. 2020;13(12):125502.
[5] von Ammon W, Dornberger E, Oelkrug H, et al. The dependence of bulk defects on the axial temperature gradient of silicon crystals during Czochralski growth. J Cryst Growth. 1995;151(3–4):273–277.
[6] Voronkov V V., Falster R. Vacancy-type microdefect formation in Czochralski silicon. J Cryst Growth. 1998;194(1):76–88.
[7] Voronkov V V., Falster R. Grown-in microdefects, residual vacancies and oxygen precipitation bands in Czochralski silicon. J Cryst Growth. 1999;204(4):462–474.
[8] Bohm J, Heimann RB, Hengst M, et al. Czochralski growth and characterization of piezoelectric single crystals with langasite structure: La3Ga5SiO14 (LGS), La3Ga5.5Nb0.5O14 (LGN), and La3Ga5.5Ta0.5O14 (LGT): Part I. J Cryst Growth. 1999;204(1–2):128–136.
[9] Trempa M, Kupka I, Kranert C, et al. Evolution of grain structure and recombination active dislocations in extraordinary tall conventional and high performance multi-crystalline silicon ingots. J Cryst Growth [Internet]. 2017;459(November 2016):67–75.
[10] Osada K, Kutsukake K, Yamamoto J, et al. Adaptive Bayesian optimization for epitaxial growth of Si thin films under various constraints. Mater Today Commun. 2020;25:101538.
[11] Miyagawa S, Gotoh K, Kutsukake K, et al. Application of Bayesian optimization for improved passivation performance in TiOx/SiOy/c-Si heterostructure by hydrogen plasma treatment. Applied Physics Express. 2021;14(2).
[12] Miyagawa S, Gotoh K, Kutsukake K, et al. Application of Bayesian optimization for high-performance TiOx/SiOy/c-Si passivating contact. Solar Energy Materials and Solar Cells [Internet]. 2021;230(April):111251.

[13] Wakabayashi YK, Otsuka T, Krockenberger Y, et al. Machine-learning-assisted thin-film growth: Bayesian optimization in molecular beam epitaxy of SrRuO3 thin films. APL Mater. 2019;7(10).
[14] Terayama K, Sumita M, Tamura R, et al. Black-Box Optimization for Automated Discovery. Acc Chem Res. 2021;54(6):1334–1346.
[15] Langner S, Häse F, Perea JD, et al. Beyond Ternary OPV: High-Throughput Experimentation and Self-Driving Laboratories Optimize Multicomponent Systems. Advanced Materials. 2020;32(14).
[16] Shimizu R, Kobayashi S, Watanabe Y, et al. Autonomous materials synthesis by machine learning and robotics. APL Mater. 2020;8(11).
[17] Müller G. Experimental analysis and modeling of melt growth processes. J Cryst Growth. 2002;237–239(1-4 III):1628–1637.
[18] Kakimoto K, Liu L. Numerical study of the effects of cusp-shaped magnetic fields and thermal conductivity on the melt-crystal interface in CZ crystal growth. Crystal Research and Technology. 2003;38(7–8):716–725.
[19] Lv G, Chen D, Yang X, et al. Numerical simulation and experimental verification of vacuum directional solidification process for multicrystalline silicon. Vacuum. 2015;116:96–103.
[20] Demina SE, Bystrova EN, Postolov VS, et al. Use of numerical simulation for growing high-quality sapphire crystals by the Kyropoulos method. J Cryst Growth. 2008;310(7–9):1443–1447.
[21] Shur JW, Kang BK, Moon SJ, et al. Growth of multi-crystalline silicon ingot by improved directional solidification process based on numerical simulation. Solar Energy Materials and Solar Cells. 2011;95(12):3159–3164.
[22] Qi X, Zhao W, Liu L, et al. Optimization via simulation of a seeded directional solidification process for quasi-single crystalline silicon ingots by insulation partition design. J Cryst Growth [Internet]. 2014;398:5–12.
[23] Keerthivasan T, Liu X, Srinivasan M, et al. The impact on mc-Si ingot grown in a directional solidification furnace by partially replacing the susceptor bottom with an insulation material: A numerical investigation. J Cryst Growth. 2023;607:127130.
[24] Tsunooka Y, Kokubo N, Hatasa G, et al. High-speed prediction of computational fluid dynamics simulation in crystal growth. CrystEngComm. 2018;20(41):6546–6550.
[25] Dang Y, Zhu C, Ikumi M, et al. Adaptive process control for crystal growth using machine learning for high-speed prediction: application to SiC solution growth. CrystEngComm. 2021;23(9):1982–1990.
[26] Isono M, Harada S, Kutsukake K, et al. Optimization of Flow Distribution by Topological Description and Machine Learning in Solution Growth of SiC. Adv Theory Simul. 2022;5(9).
[27] Liu X, Dang Y, Tanaka H, et al. Data-Driven Optimization and Experimental Validation for the Lab-Scale Mono-Like Silicon Ingot Growth by Directional Solidification. ACS Omega. 2022;7(8):6665–6673.
[28] Dropka N, Böttcher K, Holena M. Development and Optimization of VGF-GaAs Crystal Growth Process Using Data Mining and Machine Learning Techniques. Crystals (Basel). 2021;11(10):1218.
[29] Dropka N, Tang X, Chappa GK, et al. Smart Design of Cz-Ge Crystal Growth Furnace and Process. Crystals (Basel). 2022;12(12):1764.
[30] Yu W, Zhu C, Tsunooka Y, et al. Geometrical design of a crystal growth system guided by a machine learning algorithm. CrystEngComm. 2021;23(14):2695–2702.
[31] Alexander IT, Haasen P. Dislocations and plastic flow in the diamond structure. Solid State Physics. 1969;27–158.
[32] Gao B, Jiptner K, Nakano S, et al. Applicability of the three-dimensional Alexander-Haasen model for the analysis of dislocation distributions in single-crystal silicon. J Cryst Growth [Internet]. 2015;411:49–55.
[33] Boucetta A, Kutsukake K, Kojima T, et al. Application of artificial neural network to optimize sensor positions for accurate monitoring: An example with thermocouples in a crystal growth furnace. Applied Physics Express. 2019;12(12).

[34] Deb K, Pratap A, Agarwal S, et al. A fast and elitist multiobjective genetic algorithm: NSGA-II. IEEE Transactions on Evolutionary Computation. 2002;6(2):182–197.

We developed an innovative two-step optimization method for crystal growth furnaces and processes using deep neural networks to identify ideal temperature transitions and optimize furnace designs, which advances materials production environments and equipment design.

AUTHOR'S CONTRIBUTIONS

Hiroyuki Tanaka: Methodology, Investigation, Validation, Formal analysis

Kentaro Kutsukake: Conceptualization, Methodology, Writing - Review & Editing, Supervision

Kota Asakura: Validation

Takuto Kojima: Methodology

Xin Liu: Formal analysis

Noritaka Usami: Conceptualization, Writing - Original Draft, Supervision, Funding acquisition

Table I. Physical properties of silicon used for the simulation

	Si solid	Si melt
Density [kg/m^{3}]	$-3.26 \times 10^{-2}T + 2339.5$	$-0.3701T + 3194$
Emissivity	$-2.62 \times 10^{-4}T + 0.9016$	0.3
Specific heat [J/kg□K]	927	1040
Thermal conductivity [W/mK]	$5.67T^4 - 4.01T^3 + 1.0 \times 10^{-4}T$	66.5
Melting point [K]	1685	
Latent heat [J/kg]		1.81×10^6
Volume expansion coefficient [1/K]		1.36×10^{-4}
Viscosity coefficient [kg/m□s]]		8.23×10^{-4}
Young's modulus [Pa]	1.653×10^{11}	

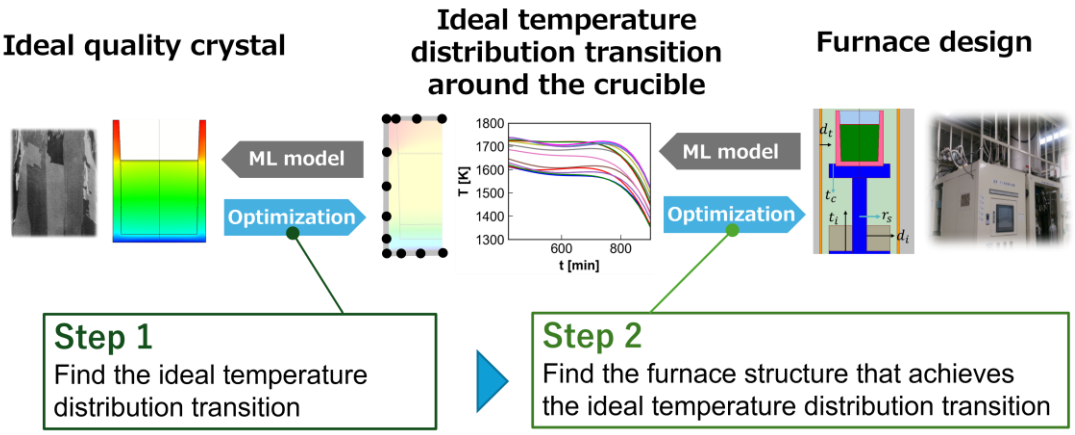

Figure 1. Schematic illustration of the two-step optimization proposed in this study.

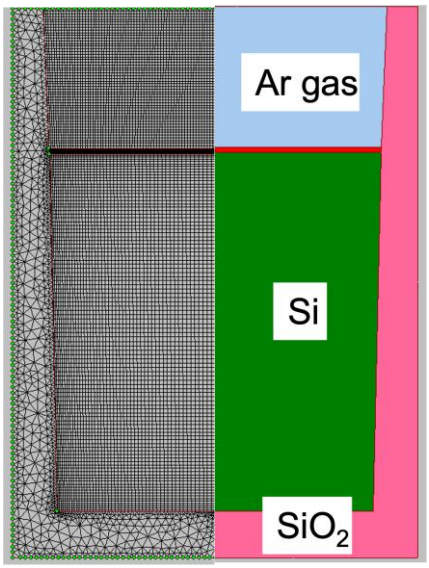

Figure 2. Schematic diagram and mesh of the crucible model, assuming Si in a crucible under Ar gas atmosphere. The surrounding area is divided into 174 sections for input of boundary conditions.

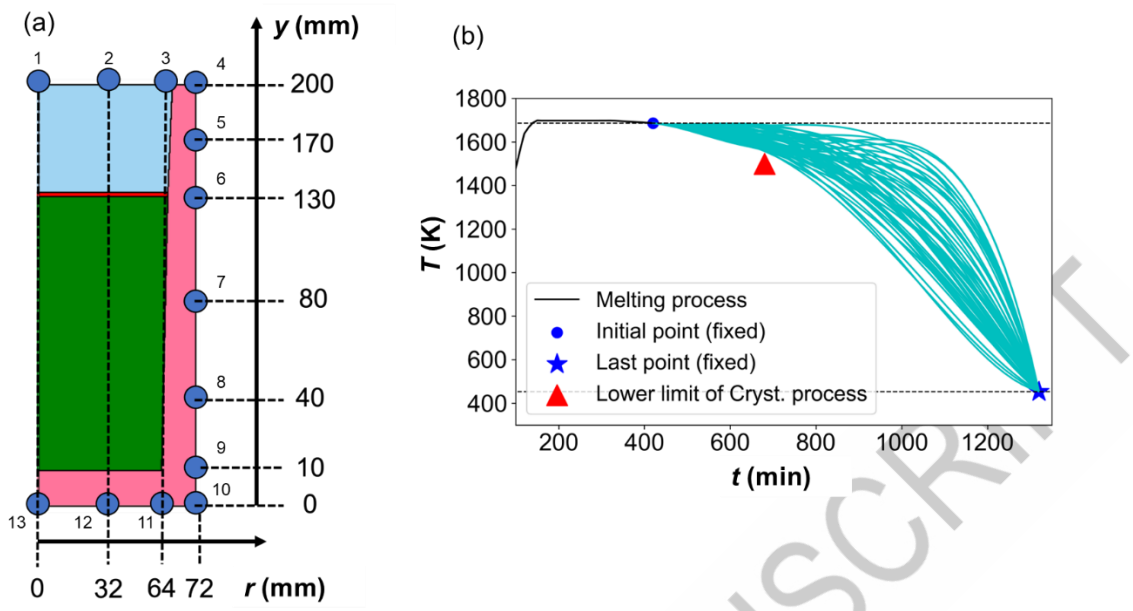

Figure 3. (a) 13 node locations and (b) A typical example of randomly generated temperature boundary conditions with a constrained quartic function in temporal transition at each node.

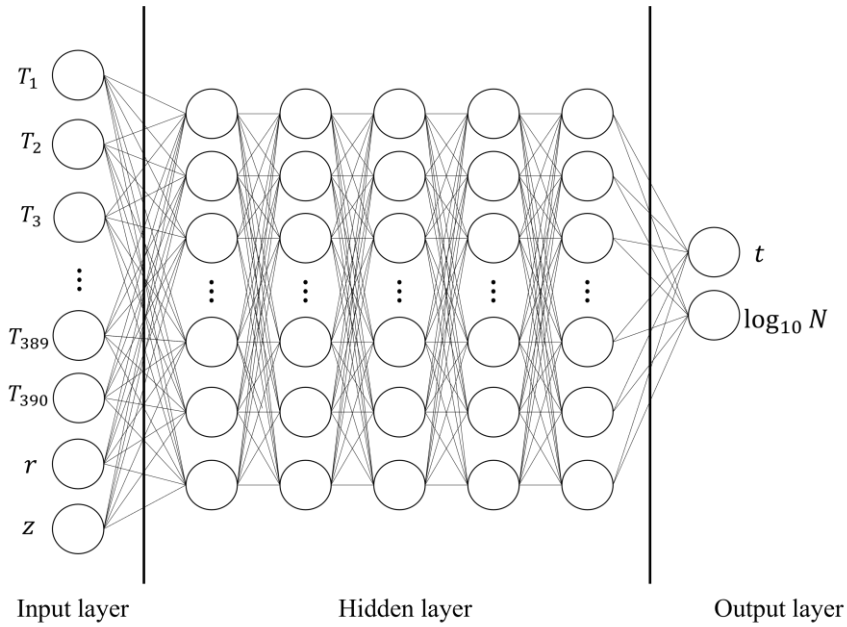

Figure 4. The structure of Model A to consists of an input layer, 5 hidden layers, and an output layer.

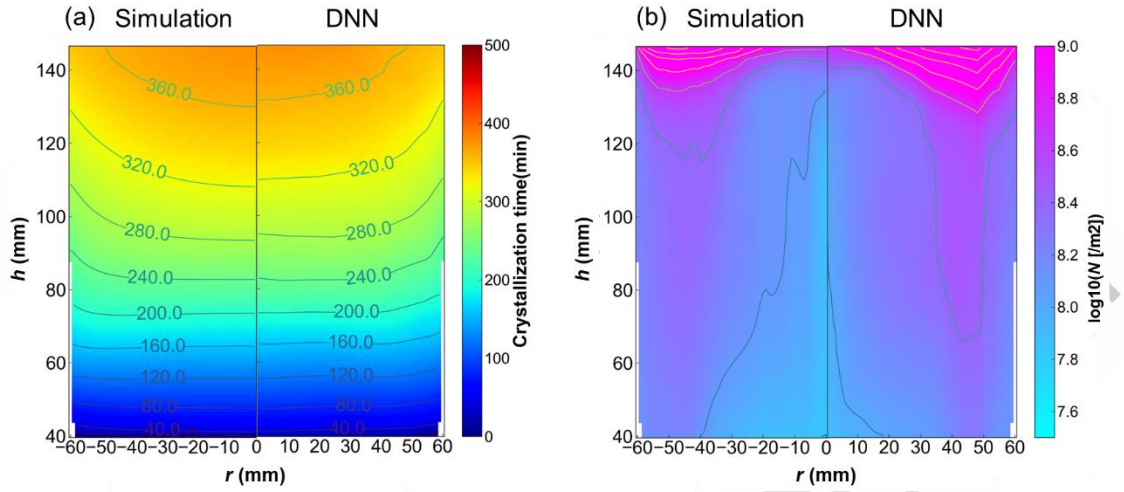

Figure 5. Comparison of simulations and predictions by DNN model A (a) Crystallization time distribution: Contour lines correspond to the transition of the solid-liquid interface shape during crystal growth. (b) Dislocation density distribution at the end of cooling.

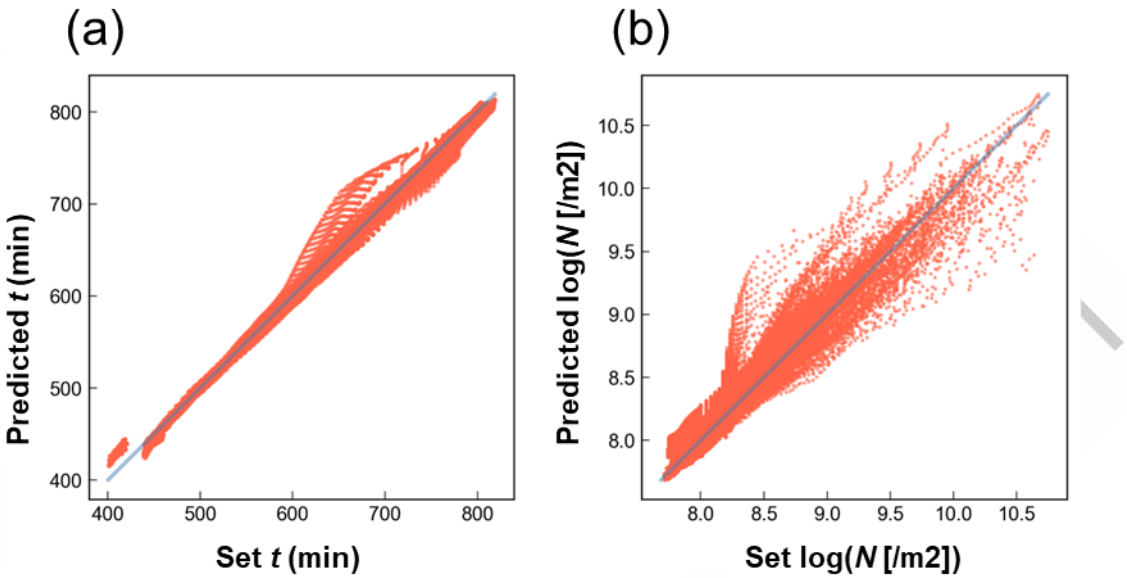

Figure 6. Parity plots for (a) crystallization time and (b) dislocation density after growth.

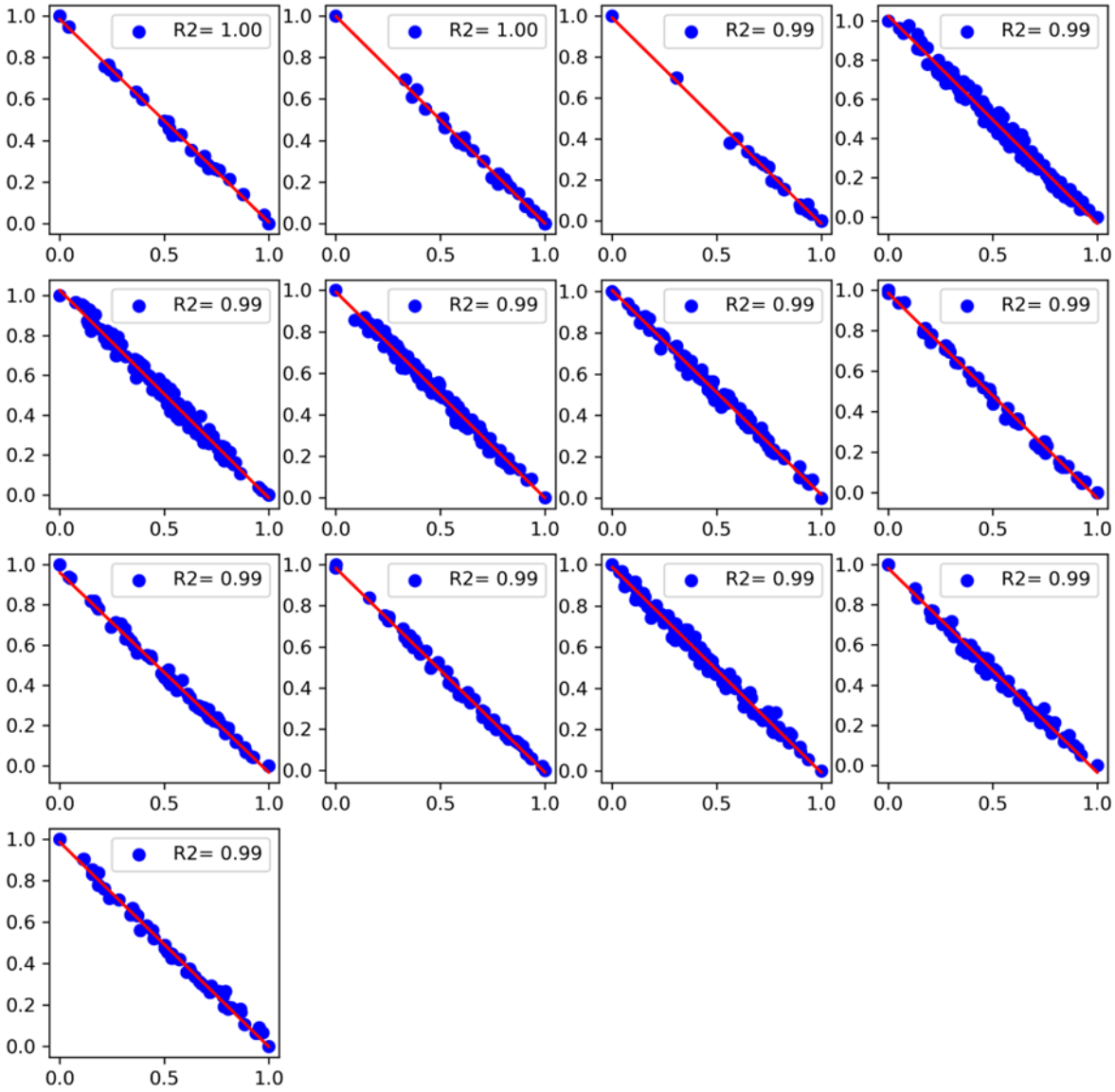

Figure 7. Pairs of polynomial coefficients after normalization at each node. The red line is the result of linear regression.

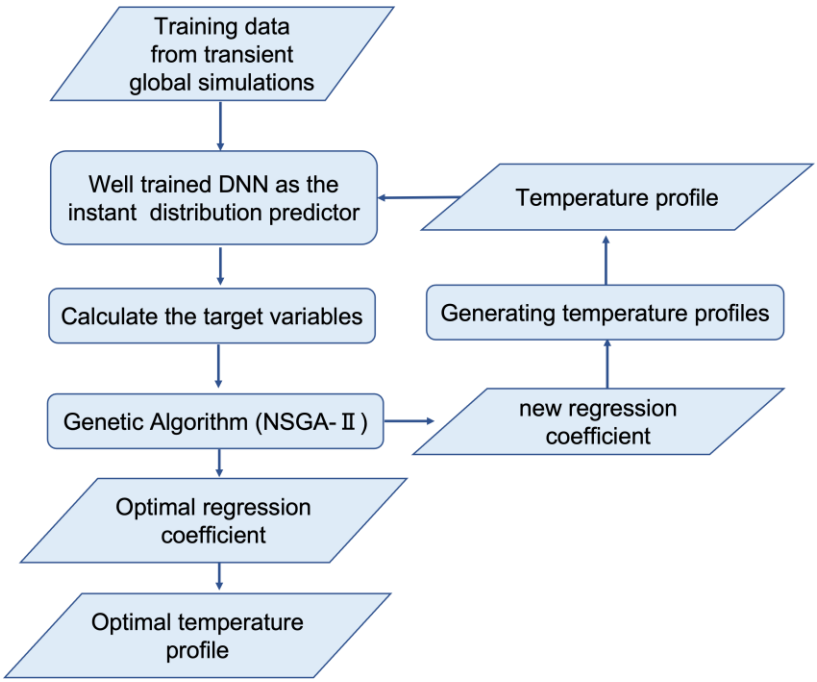

Figure 8. The workflow of GA combining DNN, where the input to the DNN is a temperature profile; the optimization parameters of the GA are polynomial coefficients tied to the temperature profile.

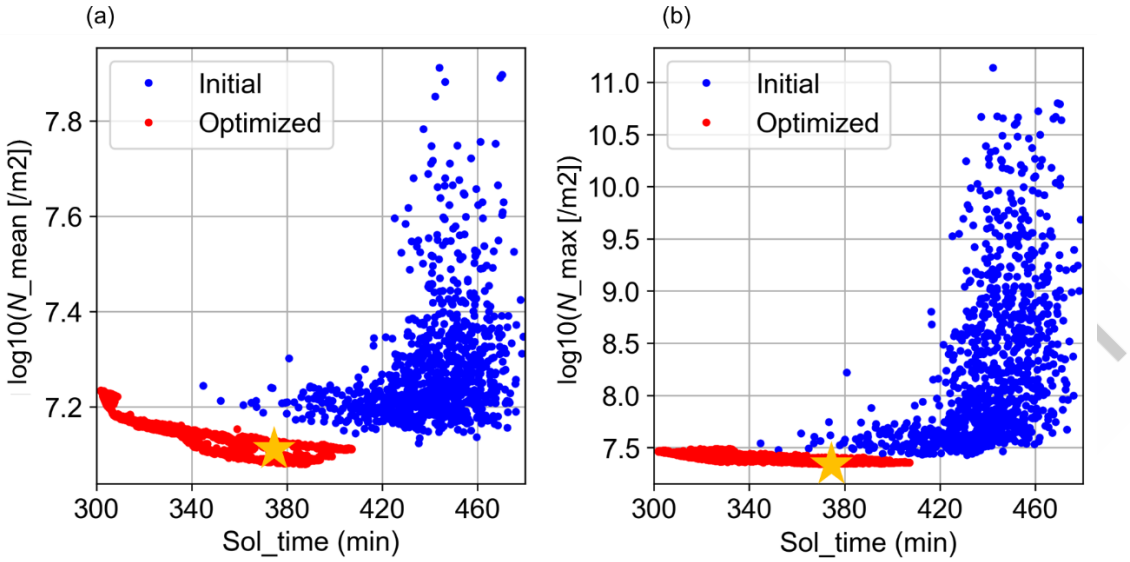

Figure 9. Pareto surfaces obtained by NSGA-II.The ★ mark in the figure was selected as the optimal solution.

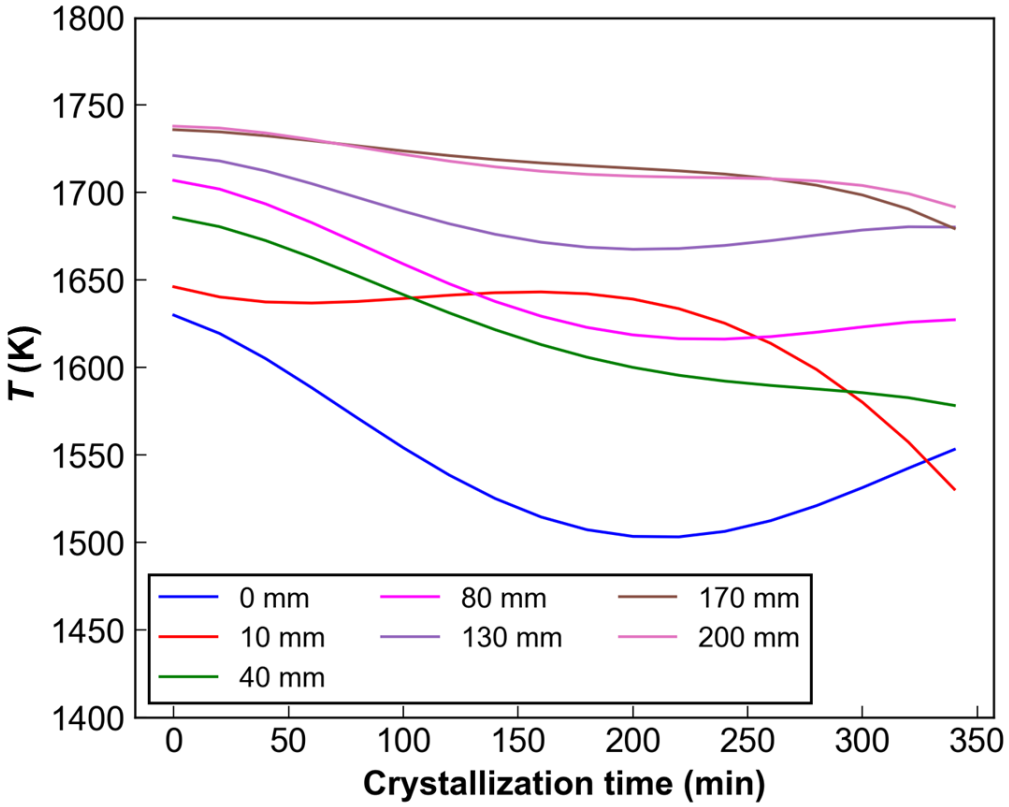

Figure 10. Optimal temperature distribution transition at the crucible side wall obtained by GA

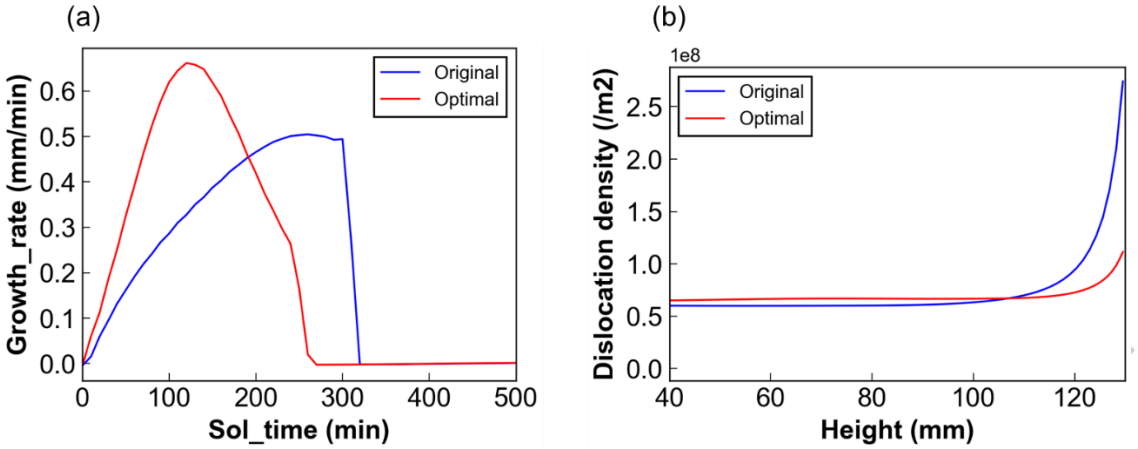

Figure 11. Comparison of (a) growth rate and (b) dislocation density at the center of the ingot using the original recipe and post-optimization results

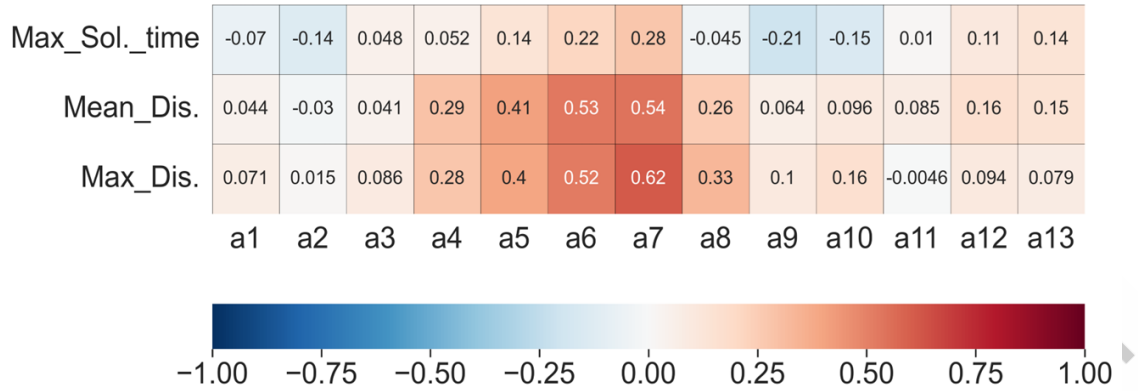

Figure 12. Correlation coefficient matrix of polynomial coefficients and objective function for each node of the training data. The correlation between the polynomial coefficients and the objective function is calculated using the normalized data.

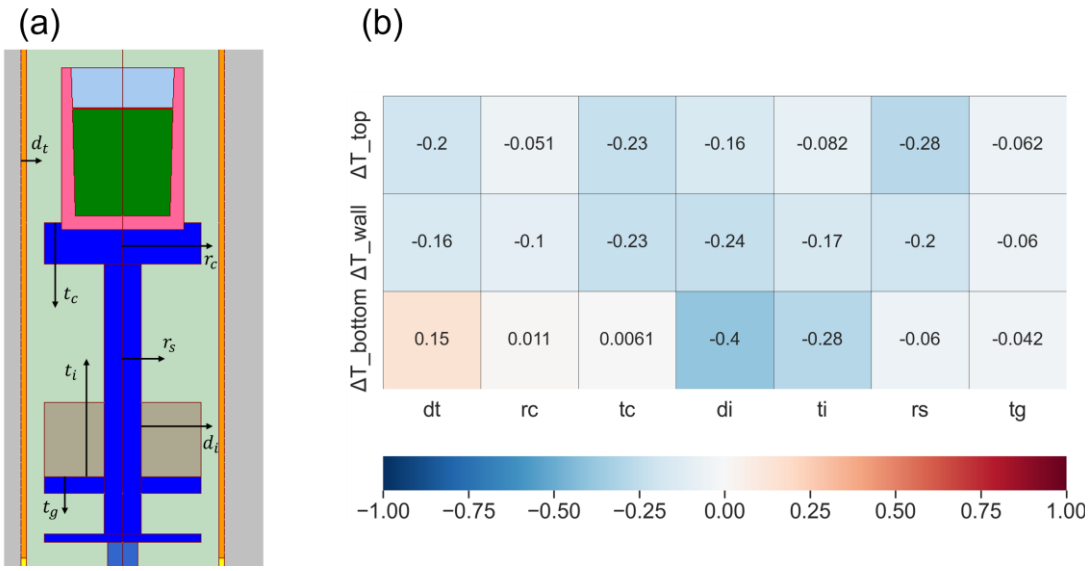

Figure 13. (a) Parameters indicating the geometry inside the crystal growth furnace and (b) standard multiple regression coefficient matrix to show the impact of the parameters on the temperatures

Table II Range of parameters related to furnace design and number of divisions when creating training data

	d_t (mm)	t_c (mm)	d_i (mm)	t_i (mm)	r_s (mm)
Range	5-10	20-80	80-100	50-150	20-60
Partitions	11	13	11	11	11

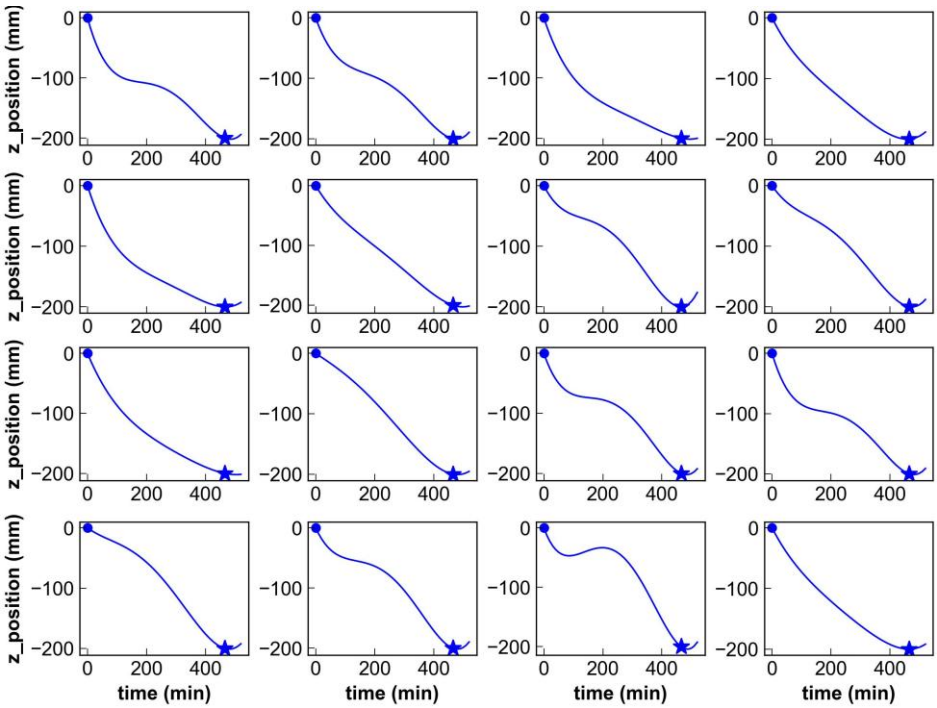

Figure 14. Time evolution of the vertical position of the crucible. The initial (●) and final (★) positions are fixed and represented as a smooth curve using a quadratic function.

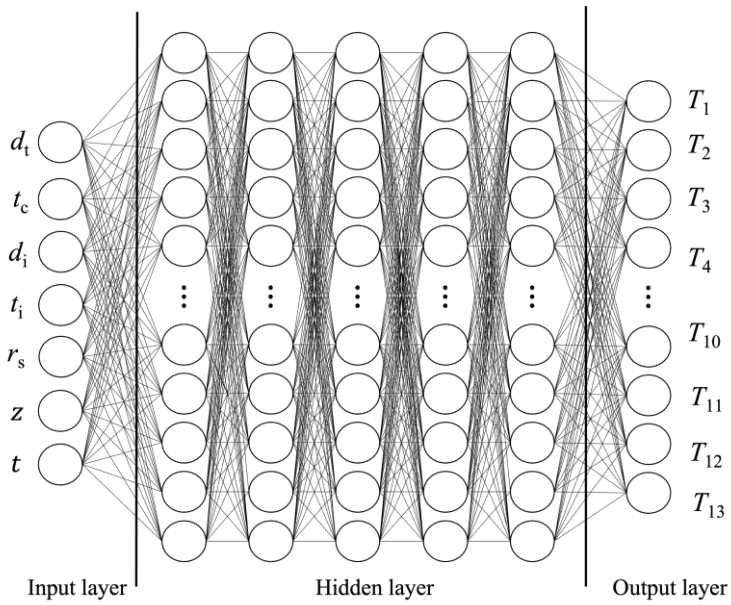

Figure 15. The structure of Model B to consist of 7 layers: input layer (7 nodes), hidden layer (50 nodes) × 5, and output layer (13 nodes).

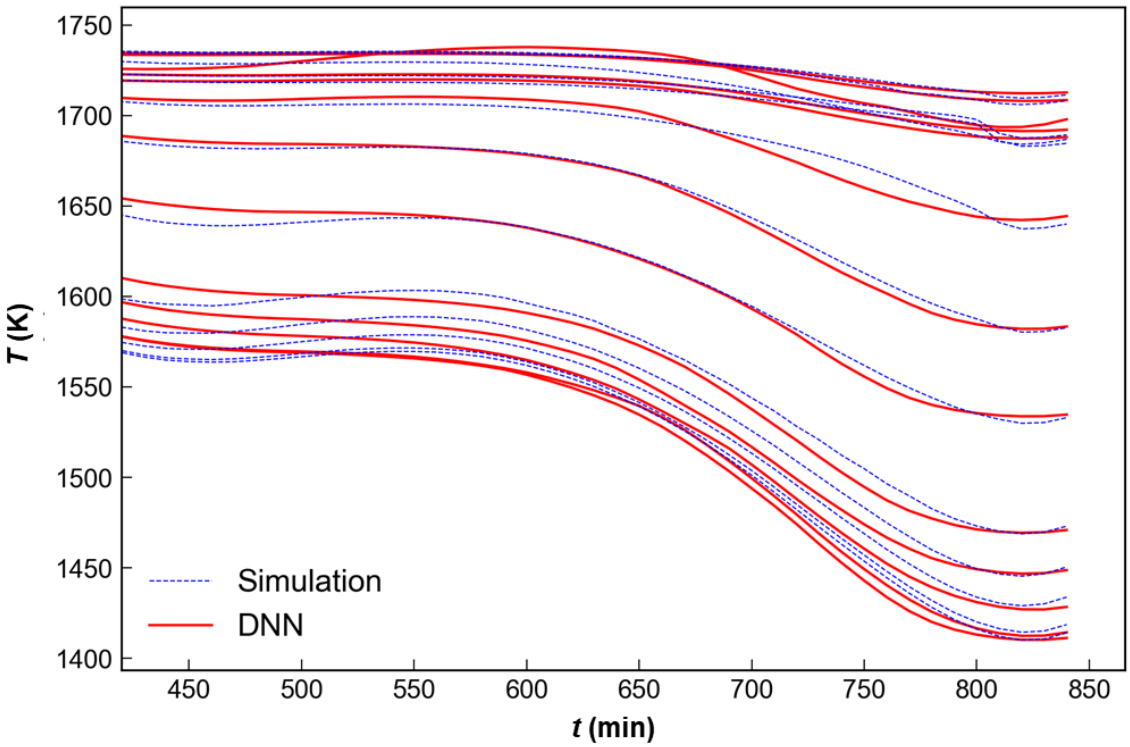

Figure 16. Comparison of simulation results and model B predictions for temperature transitions around the crucible.

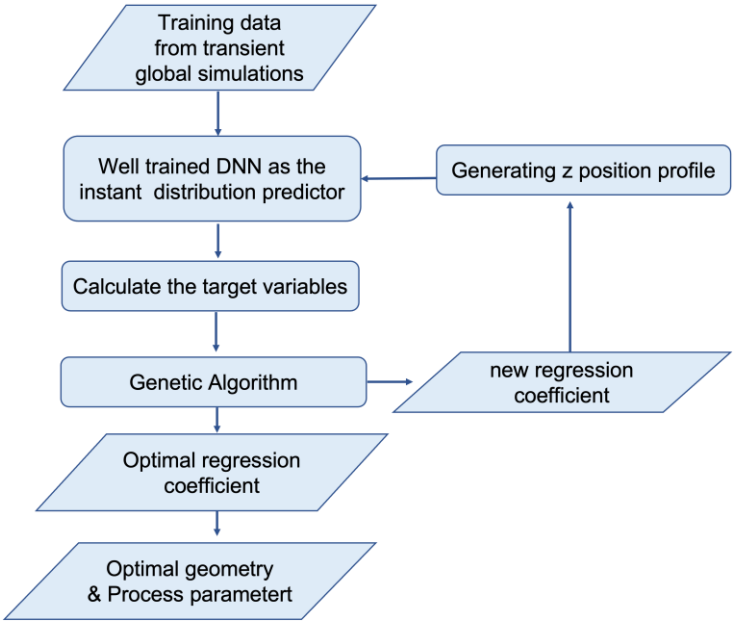

Figure 17. Workflow of GA combined with DNN; the GA optimization targets are the five parameters related to the furnace design and the polynomial coefficients tied to the vertical coordinate transition of the crucible.

Table III. Changes in parameters related to furnace design before and after optimization

	d_t (mm)	t_c (mm)	d_i (mm)	t_i (mm)	r_s (mm)
Original	7.00	50.00	96.00	91.00	22.50
Optimal	9.5846	20.00	80.08	149.9998	58.7889

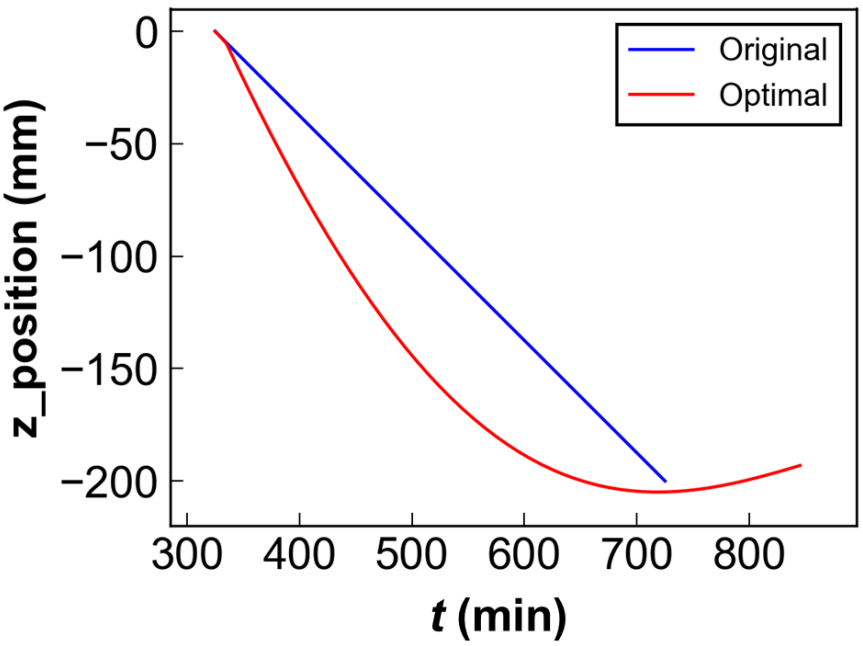

Figure 18. Comparison of the time evolution of the crucible vertical coordinates before and after optimization

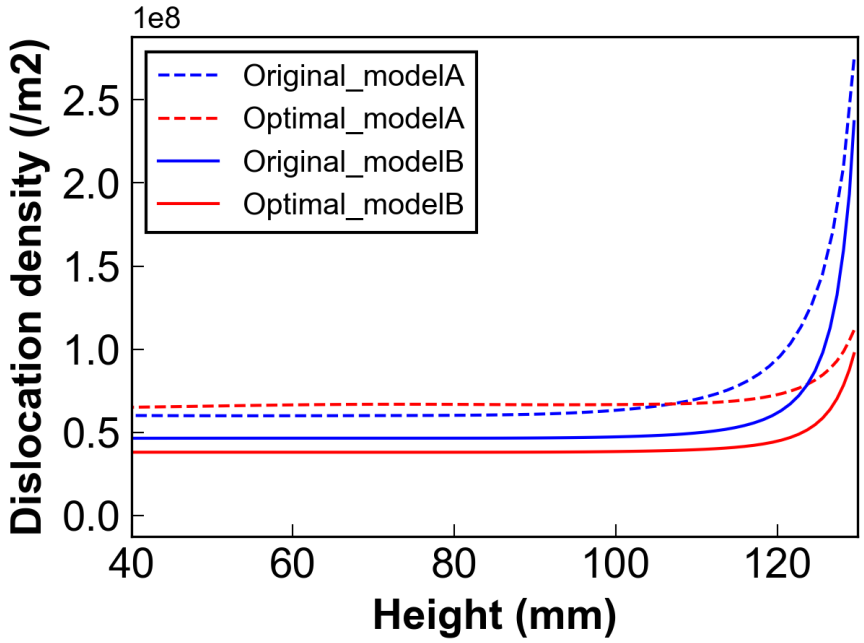

Figure 19. Dislocation densities along the center line of the ingot calculated through high-fidelity simulations incorporating stress analysis and dislocation calculations. The results of model A are the same as those in Fig. 11 (b).

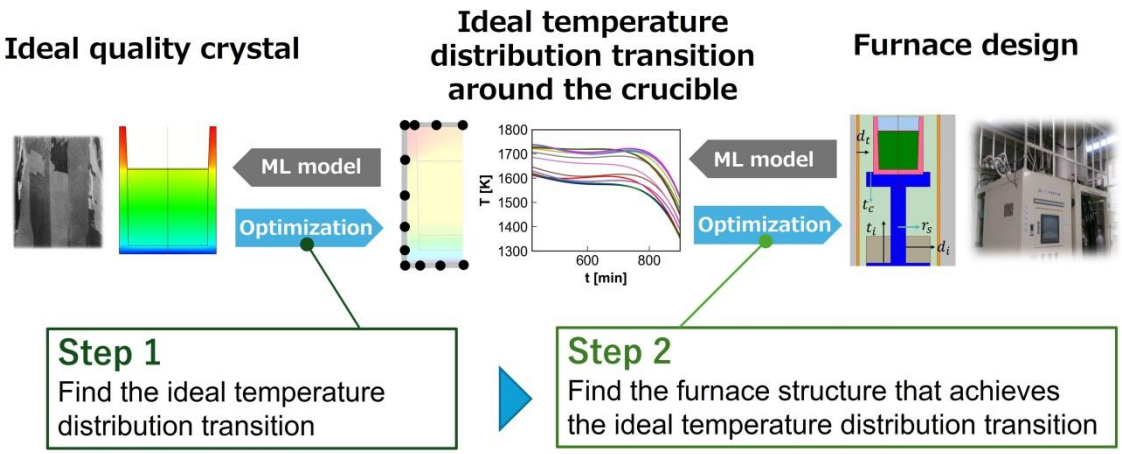

GraphicalAbstract1

Supplemental

A design methodology of crystal growth furnace and process aided by two-step optimization using machine learning models and genetic algorithm

Hiroyuki Tanaka[a], Kentaro Kutsukake[a,b,c], Kota Asakura[a], Takuto Kojima[d], Xin Liu[b], and Noritaka Usami[a,b,e*]

[a]*Graduate School of Engineering, Nagoya University, Furo-cho, Chikusa-ku, Nagoya 464-8603, Japan*

[b]*Institute of Materials and Systems for Sustainability, Nagoya University, Furo-cho, Chikusa-ku, Nagoya 464-8601, Japan*

[c] *Center of Advanced Intelligence Project, RIKEN, Tokyo 103-0027, Japan*

[d] *National Institute of Advanced Industrial Science and Technology, Tsukuba 305-8561, Japan*

[e] *Institutes of Innovation for Future Society, Nagoya University, Furo-cho, Chikusa-ku, Nagoya 464-8601, Japan*

* **E-mail: usa@material.nagoya-u.ac.jp**

Table S1. DNN accuracy of Molde A

		MSE	MAE	R2
fold1 T[K]	*t* (min)	4.639	2.769	0.998
	log10[N/(/m2)]	0.110	0.059	0.872
fold2 T[K]	*t* (min)	4.347	2.707	0.998

	log10[N/(/m2)]	0.066	0.037	0.944
fold3 T[K]	*t* (min)	6.416	3.533	0.996
	log10[N/(/m2)]	0.125	0.053	0.818
fold4 T[K]	*t* (min)	4.918	2.663	0.997
	log10[N/(/m2)]	0.118	0.053	0.881
fold5 T[K]	*t* (min)	4.473	2.843	0.998
	log10[N/(/m2)]	0.092	0.044	0.888

Table S2. DNN accuracy of Molde B

	MSE	MAE	R2
fold1 T (K) fold2	19.012	13.224	0.793
T (K) fold3 T	15.828	11.481	0.854
(K) fold4 T (K)	19.23	14.077	0.788
fold5 T (K)	21.29	14.194	0.742
	14.638	10.902	0.862

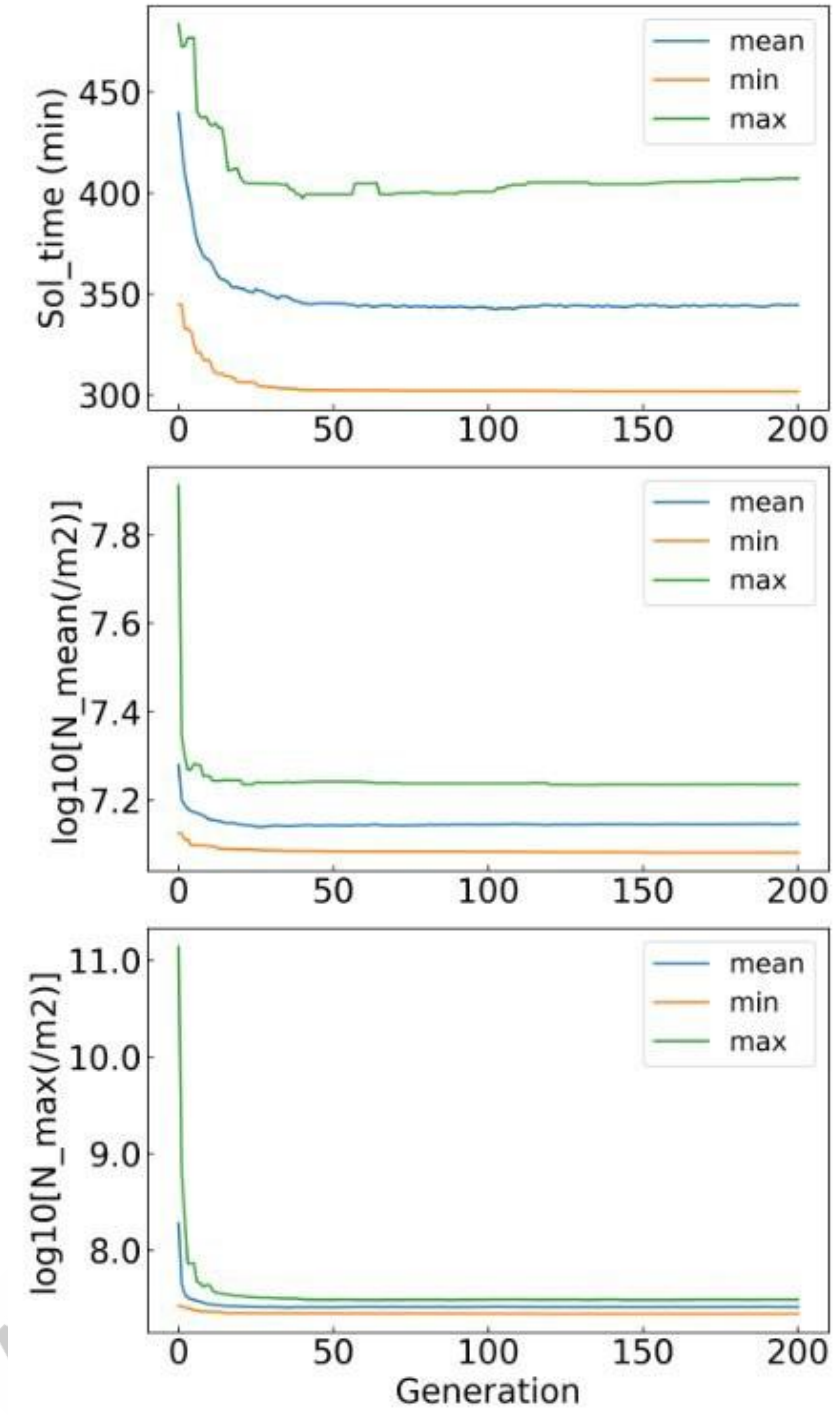

Figure S1. The progress of the three objective functions in the genetic algorithm for Model A. The solution converged sufficiently within the 200 generations.

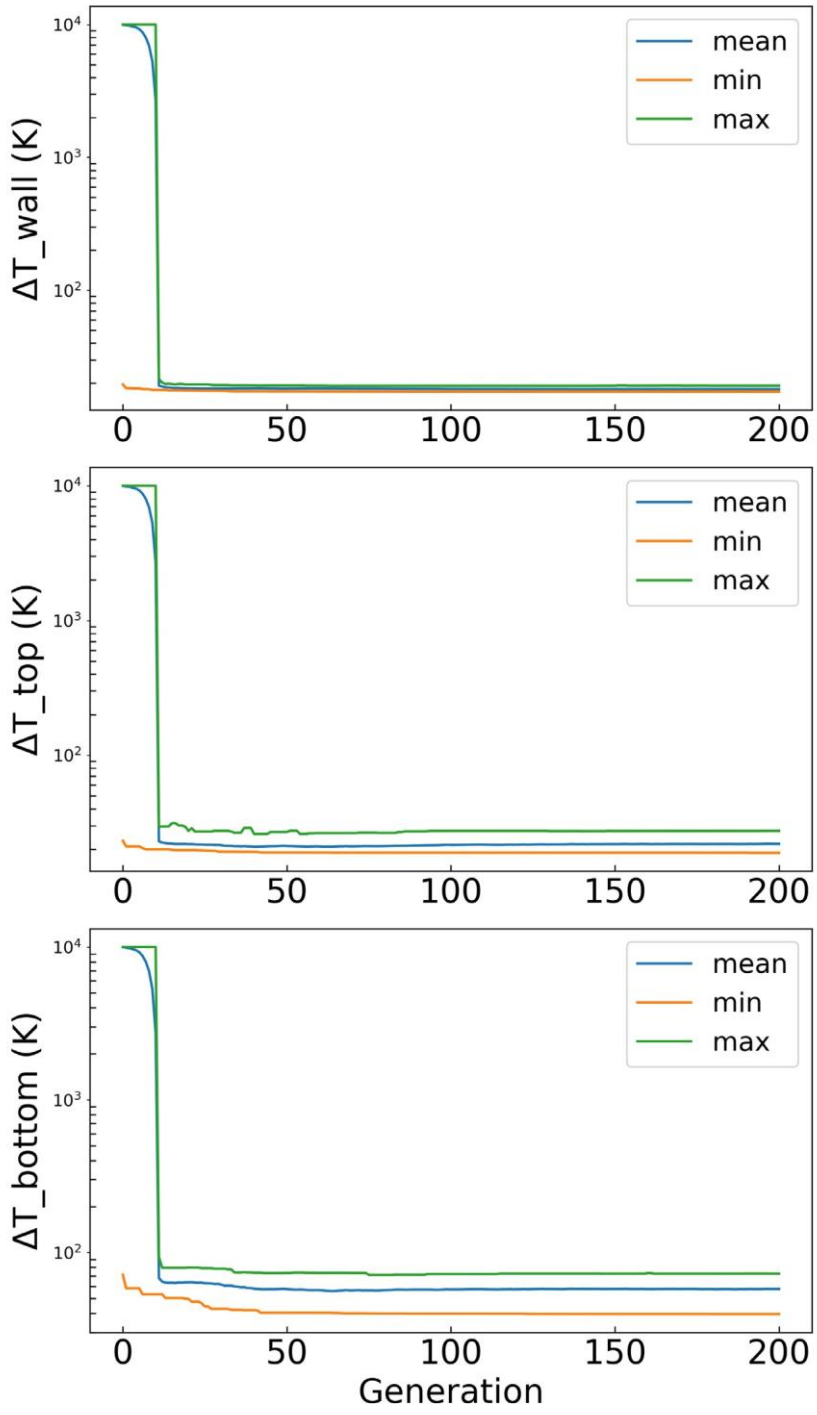

Figure S2. The progress of the three objective functions in the genetic algorithm for Model B. The solution converged sufficiently within the 200 generations.